

# Neutron stars in accreting systems – signatures of the QCD phase transition

Noshad Khosravi Largani<sup>1\*</sup>, Tobias Fischer<sup>1\*\*</sup>, Shota Shibagaki<sup>1</sup>, Pablo Cerdá-Durán<sup>2,3</sup>, and Alejandro Torres-Forné<sup>2,3</sup>

<sup>1</sup> Institute for Theoretical Physics, University of Wrocław, Plac Maksa Borna 9, 50-204 Wrocław, Poland

<sup>2</sup> Departament d’Astronomia i Astrofísica, Universitat de València, C/ Dr Moliner 50, 46100, Burjassot (València), Spain

<sup>3</sup> Observatori Astronòmic, Universitat de València, E-46980, Paterna (València), Spain

Received date / Accepted date

## ABSTRACT

Neutron stars (NS) that are born in binary systems, with a main sequence star companion, can experience mass transfer, resulting in the accumulation of material at the NS’s surface. This, in turn, leads to the continuous growth of the NS mass and the associated steepening of the gravitational potential. If the central density surpasses the onset for the phase transition from nuclear, generally hadronic matter to deconfined quark-gluon plasma—a quantity currently constrained solely from an upper limit by asymptotic freedom in QCD—the system may experience a dynamic response due to the appearance of additional degrees of freedom in the equation of state (EOS). This might give rise to a rapid softening of the EOS during the transition in the hadron-quark matter co-existence region. Whilst this phenomenon has long been studied in the context of hydrostatic configurations, the dynamical implications of this problem are yet incompletely understood. It is the essence of the present paper to simulate the dynamics of NS, with previously accreted envelopes, caused by the presence of a first-order QCD phase transition. Therefore, the neutrino radiation hydrodynamics treatment is employed based on the fully general relativistic approach in spherical symmetry, implementing three-flavor Boltzmann neutrino transport and a microscopic model EOS that contains a first-order hadron-quark phase transition. The associated neutrino signal shows a sudden rise of the neutrino fluxes and average energies, becoming observable for the present generation of neutrino detectors for a galactic event, and a gravitational wave mode analysis reveals the behaviors of the dominant  $f$  and first gravity  $g$  modes that are being excited during the NS evolution across the QCD phase transition.

**Key words.** Stars: neutron – Equation of state – Dense matter – Neutrinos – Gravitational waves

## 1. Introduction

Accreting neutron stars (NS) in binary systems have long been considered subjects of gravitational wave (GW) emission (c.f. [Wagoner, 1984](#)), e.g., through ellipticity and internal oscillations, which has been studied extensively in the context of low-mass X-ray binary systems by [Watts et al. \(2008\)](#) with potential future GW detection prospects (see also [Andersson et al., 2011](#)). Unstable oscillation modes have been studied too in the context of accreting NS (c.f. [Lasky, 2015](#), and references therein) as well as GW emission due to star quakes (see [Ruderman, 1969](#); [Giliberti & Cambiotti, 2022](#), and references therein) and in addition due to high magnetic fields (c.f. [Bonazzola & Gourgoulhon, 1996](#), and references therein); for recent works about magnetically deformed NS, see [Haskell et al. \(2008\)](#) and [Singh et al. \(2020\)](#). One of the largest uncertainties in all these considerations is the yet-incompletely understood equation of state (EOS), concerning the NS crust, especially the stability of the crust ([Chamel & Haensel, 2008](#)), as well as the high-density phase in excess of nuclear saturation density. In particular, the latter concerns the presence of hadronic resonances as well as a transition to the quark-

gluon plasma. From numerical solutions of quantum chromodynamics (QCD), the theory of strong interactions with quarks and gluons as fundamental degrees of freedom, a cross-over transition occurs at a pseudocritical temperature, in the range of 150–160 MeV, and at vanishing baryon density (c.f. [Bazavov et al., 2019](#)). Even though perturbative QCD has been probed useful to potentially constrain the high-density EOS for compact stars (c.f. [Kurkela et al., 2014](#); [Annala et al., 2020](#), and references therein), the conditions encountered at the NS interior correspond to the non-perturbative regime of QCD and hence phenomenological quark matter models have commonly been employed in astrophysical studies. These assume a first-order transition with a phase transition construction from a given hadronic model EOS ([Glendenning, 2012](#)). Observations of NS glitches, c.f. [Espinoza et al. \(2011\)](#), is one example that has been speculated to be related to possible phase transitions at the NS interior, e.g., due to the appearance of deconfined QCD degrees of freedom as well as a transition to a state of superfluidity have been investigated (for classical works, see [Anderson & Itoh, 1975](#); [Alpar et al., 1984](#), and references therein); for a comprehensive review about the possible mechanisms for glitches, see [Haskell & Melatos \(2015\)](#).

\* *email:* noshad.khosravilargani@uwr.edu.pl

\*\* *email:* tobias.fischer@uwr.edu.pl

Complementary, methods of NS asteroseismology have long been explored in the context of compact stars, implementing linear perturbation theory (see [Andersson & Kokkotas, 1998](#), and references therein) in order to predict possible GW emission characteristics. Such an approach has been demonstrated to provide reliable frequency estimates for the dominant modes, known as  $f$  mode, as well as for gravity  $g_l$  modes and pressure  $p_l$  modes. While the former has been referred to the damping of oscillations (c.f. [Benhar et al., 2004](#)), the presence of  $g$  (transverse) and  $p$  (longitudinal) modes are related to buoyancy and sound waves, respectively. Furthermore, asteroseismology has been proposed as a tool to probe the stellar properties, which implies the EOS. This has been done by [Sotani et al. \(2012\)](#) for NS and for proto-NS by [Sotani & Takiwaki \(2016\)](#) [Sotani et al. \(2017\)](#), [Torres-Forné et al. \(2018\)](#), and [Torres-Forné et al. \(2019b\)](#) as well as in [Sotani & Sumiyoshi \(2019\)](#) toward black-hole formation in failed core-collapse supernovae (see also [Cerdá-Durán et al., 2013](#)). In addition, various universal relations of NS bulk properties have been studied to remove the EOS dependence, e.g., relating the maximum mass and corresponding radii of rapidly and non-rotating configurations as well as the moment of inertia and NS tidal deformability (for a recent review, see [Yagi & Yunes, 2017](#), and references therein), extending also to finite temperature studies ([Raduta et al., 2020](#); [Khosravi Largani et al., 2022](#)). Universal relations have also been suggested to exist for several GW modes deduced from detailed asteroseismology analyses in the content of NS in [Sotani & Kumar \(2021\)](#) and for proto-NS by [Torres-Forné et al. \(2019a\)](#), [Warren et al. \(2020\)](#), [Sotani et al. \(2021\)](#) and [Mori et al. \(2023\)](#). These studies, despite some tension about the exact dependencies, e.g., surface gravity and mean density, will eventually reveal details about the EOS from future GW detections.

A detailed analysis within the context of QCD phase transitions at the NS interior has been considered within general relativistic hydrodynamics simulations of isolated NS in axial symmetry by [Dimmelmeier et al. \(2009\)](#), where the phase transition occurs due to the loss of angular momentum, and in hydrostatic models by [Sotani & Kojo \(2023\)](#) probing the high-density EOS. The latter study found that the configurations with quark matter at their interior have generally lower dominant  $f$ -mode frequencies, by several 100 Hz, compared to the hadronic reference case, depending on the compact star’s mass. On the other hand, hydrodynamical simulations, featuring a first-order QCD phase transition, have been performed extensively in the context of core-collapse supernovae ([Sagert et al., 2009](#); [Fischer et al., 2011, 2018](#)) and binary neutron star mergers ([Bauswein et al., 2019](#); [Most et al., 2019](#)). Special emphasis has been in these studies on predictions for potentially observable multi-messenger signals in neutrino and GW emissions (see also [Zha et al., 2020](#); [Kuroda et al., 2022](#)) as well as to constrain bulk properties from a potential future observation of the core-collapse supernova neutrino signal in [Khosravi Largani et al. \(2023\)](#) and the binary NS merger GW signals in [Blacker et al. \(2020\)](#). [Kuroda et al. \(2022\)](#) found loud core-collapse supernova GW signals from the first-order QCD phase transition with frequencies in the range of several kHz with amplitudes in excess of the ordinary neutrino-driven supernova explosions and even of black hole formation.

In this article, we extend the study of [Sotani & Kojo \(2023\)](#) by performing neutrino radiation hydrodynamics simulations of NS in accreting systems as an alternative astrophysical scenario to probe a possible QCD phase transition. A well calibrated nuclear matter EOS from [Hempel & Schaffner-Bielich \(2010\)](#) based on the DD2F relativistic mean field parametrization of [Typel et al. \(2010\)](#), with density-dependent nucleon-meson couplings, is implemented together with a first-order phase transition to the quark-gluon plasma based on the relativistic density function EOS of [Bastian \(2021\)](#). The resulting hybrid EOS is consistent with present nuclear physics constraints such as nuclear saturation properties and the supersaturation density constrain derived from the elliptic flow analysis of heavy-ion collision experiments by [Danielewicz et al. \(2002\)](#), as well as astrophysical constraints derived from observations of pulsar timing.

From population synthesis it is presently understood that about 30–50% of massive stars are in binary systems (c.f. [Eldridge, 2017](#), and references therein), some of which result in high-mass X-ray binaries (c.f. [Tauris & van den Heuvel, 2006](#), and references therein). Even though binary stellar evolution predicts potentially very different tracks for single- and binary-star systems (c.f. [Sana et al., 2012](#)), it is natural to assume that some of the binary systems will end up having a NS, i.e. after the first core-collapse supernova explosion took place and a main sequence companion star. The latter can well be a low- or intermediate-mass star. The lifetime of such systems depends on the properties of the system, e.g., age, metallicity, geometry such as the spatial separation and angular velocities as well as that of the companion star such as its mass. If the binary system’s configuration enables mass transfer from the companion star onto the NS, also in particular if a common envelope phase occurs ([Keegans et al., 2019](#)), which is enabled when Roche-Lobe overflow occurs (c.f. [Tauris et al., 2013](#), and references therein).

The details leading to accreting NS systems are left aside in the present investigation. Instead, it is considered that a NS has undergone mass transfer for a certain period and further, that mass accretion has ceased. This is similar to what is considered in accreting white dwarf systems leading to Novae ([Chomiuk et al., 2021](#)). Furthermore, it is expected that mass transfer from the companion star heats the neutron star’s surface and, to a lesser extent, the NS interior. In excess of temperatures of several  $10^9$  K ( $T = 6 \times 10^9$  K corresponding to 0.517 MeV), neutrinos are being produced from a variety of weak reactions. Taking those into account in the simulations, featuring three-flavor Boltzmann neutrino transport allows for the prediction not only of the neutrino fluxes and their spectra but to study also the potential impact on mass ejection associated with the NS evolution.

The manuscript is organized as follows. In sec. 2 the simulation setup is introduced, followed by the discussion of the neutrino radiation hydrodynamics simulations in sec. 3, including the neutrino emission. Sec. 4 discusses the GW mode analysis. The paper closes with a summary in sec. 5.

## 2. Equation of state and initial conditions

For the construction of the initial conditions for the numerical study of systems that are composed of neutron stars with previously accreted envelopes, the hadronic EOS cat-

analog of Hempel et al. (2012) is employed together with the relativistic density functional (RDF) quark-matter hadron EOS catalog of Bastian (2021), both of which are available as multi-purpose tabulations for astrophysical application at the CompOSE EOS database<sup>1</sup>. For the hadronic EOS, the DD2F relativistic mean field (RMF) model of Typel et al. (2010) is selected, and for the quark-hadron EOS the DD2F-RDF-1.1 parametrization is employed representative for the entire class of RDF models. At densities below normal nuclear matter density<sup>2</sup> and low temperatures, the RMF EOS is extended into the modified nuclear statistical equilibrium (NSE) model of Hempel & Schaffner-Bielich (2010) with several thousand nuclear species (for a review of this class of hadronic EOS in supernova simulations, see Fischer et al., 2017, and references therein). Figure 1 (left panel) compares these two EOS at the condition of  $\beta$ -equilibrium and for two constant values of the entropy per baryon of  $s = 0.1 k_B$  and  $s = 0.5 k_B$ .

The DD2F-RDF-1.1 hybrid EOS of Bastian (2021) implements a first-order hadron-quark phase transition from the DD2F hadronic EOS. At the present conditions of  $s = 0.5 k_B$  an onset density for the phase transition is obtained of  $\rho = 8.8 \times 10^{14} \text{ g cm}^{-3}$  and an onset mass of  $1.582 M_\odot$ , as is illustrated via the horizontal grey line in the right panel of Fig. 1. Note that the EOS bulk property differences for different entropies in the range of  $s = 0.1$ – $0.5 k_B$ , and  $T = 0$  configurations are on the order of one percent (see Table I in Bastian, 2021). Larger differences arise on the phase transition region, as is illustrated in the left panel in Fig. 1, comparing the  $T = 0$  and  $s = 0.5 k_B$  cases where the onset density for the phase transition decreases as well as the change of the pressure slope is less abrupt for the finite entropy situation. This feature of the RDF class of hadron-quark matter hybrid EOS has been discussed in detail in the example of core-collapse supernova simulations in Fischer et al. (2018), Fischer (2021) and recently in Khosravi Largani et al. (2023), as well as for (non)rotating hot and cold NS in Khosravi Largani et al. (2022), however, for somewhat larger entropies of  $s = 3 k_B$  leaving a stronger impact on the hybrid (proto)NS maximum mass and radius.

The quark matter phase of the RDF EOS is based on the concept of the string-flip model, originally developed by Goddard et al. (1973) and Johnson & Thorn (1976), and later further extended by Röpke et al. (1986) and Horowitz et al. (1985). It mimics confinement through divergent medium-dependent quark masses, which has been extended recently for applications to hydrodynamical simulations of heavy-ion collisions in Bastian et al. (2023). Of particular relevance for astrophysics are repulsive interactions, implemented here through leading and higher order vector interaction channels, following Benić et al. (2015) and Kaltenborn et al. (2017), similar as is the case in simplistic quark-matter model EOS of the Nambu–Jona-Lasinio type (Nambu & Jona-Lasinio, 1961) as well as vector-interaction enhanced bag models of Klähn & Fischer (2015). These are essential in order to obtain maximum neutron star masses—hybrid stars if quark matter is present at their interior—consistent with the current constraints of the maximum

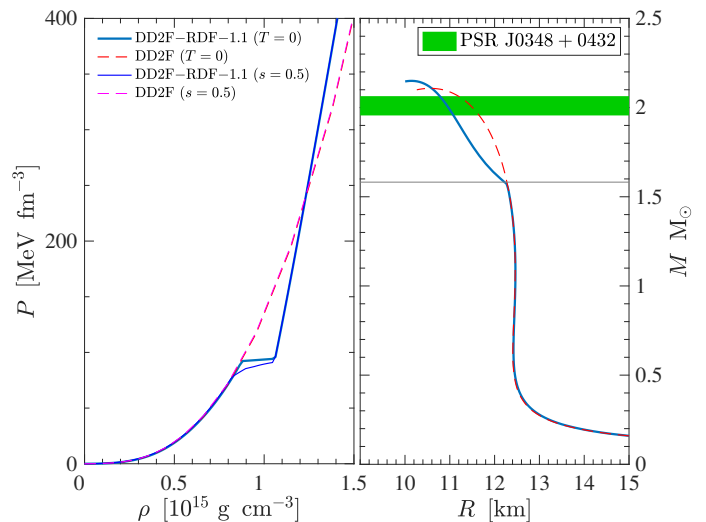


**Fig. 1.** Comparison of the EOS at  $\beta$ -equilibrium for zero temperature ( $T = 0$ ) and for a constant entropy per particle of  $s = 0.5 k_B$ , for DD2F-RDF-1.1 (solid light and dark blue lines) and DD2F (dashed red and magenta lines), in comparison to the corresponding DD2F hadronic EOS (red and magenta dashed lines respectively, which lay on top of each other for both configurations), showing pressure  $P$  versus restmass density  $\rho$  (left panel) and the mass  $M$  radius  $R$  relation (right panel), including as example the high-precision maximum mass constraint of  $2.01 \pm 0.04 M_\odot$  (light grey band) deduced from the radio observations of PSR J0348+0432 of Antoniadis et al. (2013). The horizontal grey line in the mass-radius diagram marks the onset mass for the quark-hadron phase transition at  $M = 1.582 M_\odot$  for the EOS with  $s = 0.5 k_B$ .

mass of about  $2 M_\odot$  deduced from high-precision radio observations (c.f. Antoniadis et al., 2013; Fonseca et al., 2021). The DD2F-RDF-1.1 hybrid EOS features a maximum mass of  $2.150 M_\odot$  for  $s = 0.5 k_B$  and  $2.155 M_\odot$  for  $T = 0$  (for a detailed discussion about the differences of finite entropy per particle and  $T = 0$  NS and hybrid stars, see Khosravi Largani et al., 2022).

Precision NS radius constraints are available since the observation analysis of quiescent low-mass X-ray binaries by Steiner et al. (2010), with  $R = 11$ – $12$  km for intermediate-mass neutron stars of  $M \simeq 1.4 M_\odot$ . These constraints have been further strengthened due to the analysis of the GW data from the binary neutron star merger event GW170817, provided by Abbott et al. (2018) and re-analyzed by De et al. (2018) taking into account the binary NS mass ratio. Further, high-precision NS radii constraints are available from the NICER NASA mission, consistent with the present DD2F-RDF-1.1 EOS. The radii of massive neutron stars of around  $2.0 M_\odot$  is  $R_{2.0} = 11.1$  km, in agreement with the values derived by Riley et al. (2021) and Miller et al. (2021), and that of  $1.5 M_\odot$  intermediate-mass NS is  $R_{1.5} = 12.4$  km, in agreement with the analysis of Bilous et al. (2019) and Miller et al. (2019).

Initial conditions are constructed for the hydrodynamical simulations of NS with an accreted envelope. Therefore, hydrostatic NS solutions, based on the Tolmann–Oppenheimer–Volkov equations, are computed for a NS of selected baryon mass of  $M = 1.781 M_\odot$  based on the

<sup>1</sup> The EOS data and routines provided by CompOSE can be downloaded from the web site <https://compose.obspm.fr>

<sup>2</sup> The saturation density for DD2F is  $0.145 \text{ fm}^{-3}$  or equivalently in cgs units,  $2.44 \times 10^{14} \text{ g cm}^{-3}$

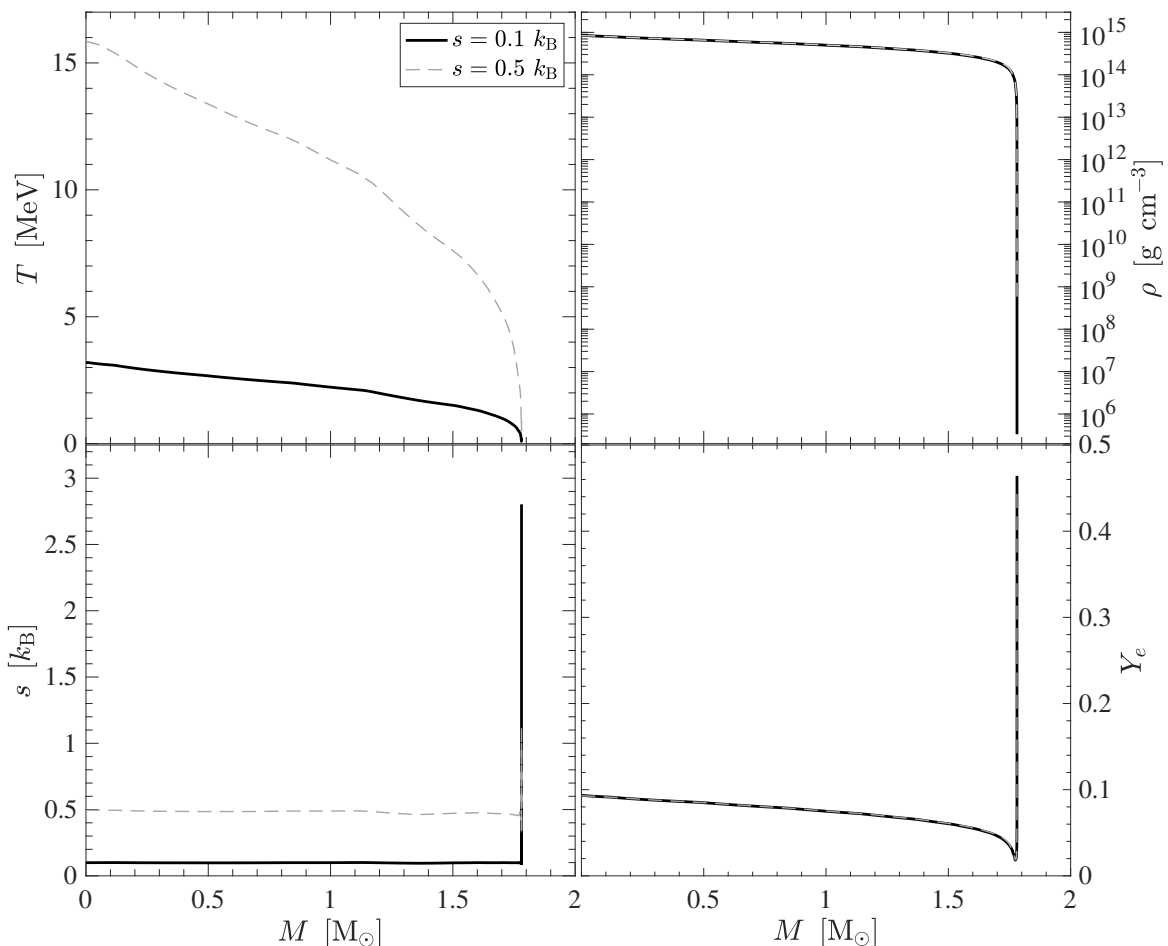


**Fig. 2.** Initial conditions for the NS simulations, based on the DD2F-RDF-1.1 hadron-quark hybrid EOS, for a NS with total baryon mass of  $M = 1.781 M_{\odot}$  (corresponding to a gravitational mass of  $M_G = 1.588 M_{\odot}$ ), showing the temperature  $T$  in the upper left panel, restmass density  $\rho$  in the upper right panel, entropy per baryon  $s$  in the lower left panel, and electron abundance  $Y_e$  in the lower right panel, as a function of the enclosed baryon mass. We compare two configurations, with constant central entropy of  $s = 0.1 k_B$  (black solid lines) and  $s = 0.5 k_B$  (grey dashed lines).

hadronic DD2F EOS. It corresponds to a gravitational mass of  $M_G = 1.588 M_{\odot}$ . A constant central entropy of  $s = 0.1 k_B$  is assumed and compared with a configuration of  $s = 0.5 k_B$  in Fig. 2, showing the corresponding radial profiles of selected quantities as a function of the enclosed baryon mass  $M$ . It becomes evident that the structure of the NS is independent of all thermodynamic quantities, such as the restmass density and  $Y_e$ , for this entropy range, except central temperatures, which vary between about 3 and 16 MeV, respectively (lower left panel in in Fig. 2). However, the thermal contributions to the high-density EOS are negligible, such that both configurations have the same central densities of  $\rho = 8.5 \times 10^{14} \text{ g cm}^{-3}$  (upper right panel in Fig. 1). Towards the star’s surface, the temperature decreases towards around  $T = 0.5 \text{ MeV}$ , and the electron abundance (lower right panel) increases from the minimum value of  $Y_e = 0.018$  towards values of  $Y_e = 0.4642$  at the lowest density considered in this study. For simplicity, in the hydrodynamical simulations, matter is assumed to be in nuclear statistical equilibrium everywhere in the NS envelope and crust, which, according to modified NSE EOS of Hempel & Schaffner-Bielich (2010), gives  $^{56}\text{Ni}$  as the nuclear composition. The NS crust-core transition is

therefore implemented via the excluded volume approach, constructing therefore a first-order phase transition, which ensures the disappearance of all nuclei at nuclear saturation density. A comparison of this approach with other, microscopic nuclear calculations has been discussed in Fischer et al. (2020b).

An accreted envelope is assumed to contain  $M_{\text{envelope}} = 0.018 M_{\odot}$ , constructed such that the resulting NS, with  $M_G = 1.588 M_{\odot}$ , belongs to the hybrid branch in the mass-radius diagram. Note that the onset mass is  $1.57 M_{\odot}$  for the DD2F-RDF-1.1 EOS (see Table I in Bastian, 2021). The continues mass transfer from the secondary companion star is expected to gradually heat the stellar interior as the gravitational potential steepens continuously during this process, for which we select the aforementioned values of central entropy. However, the entropy of the outer parts of the envelope rises sharply at low density, reaching values up to  $s = 1\text{--}3 k_B$ , see Fig. 1, which is dominated by radiation.

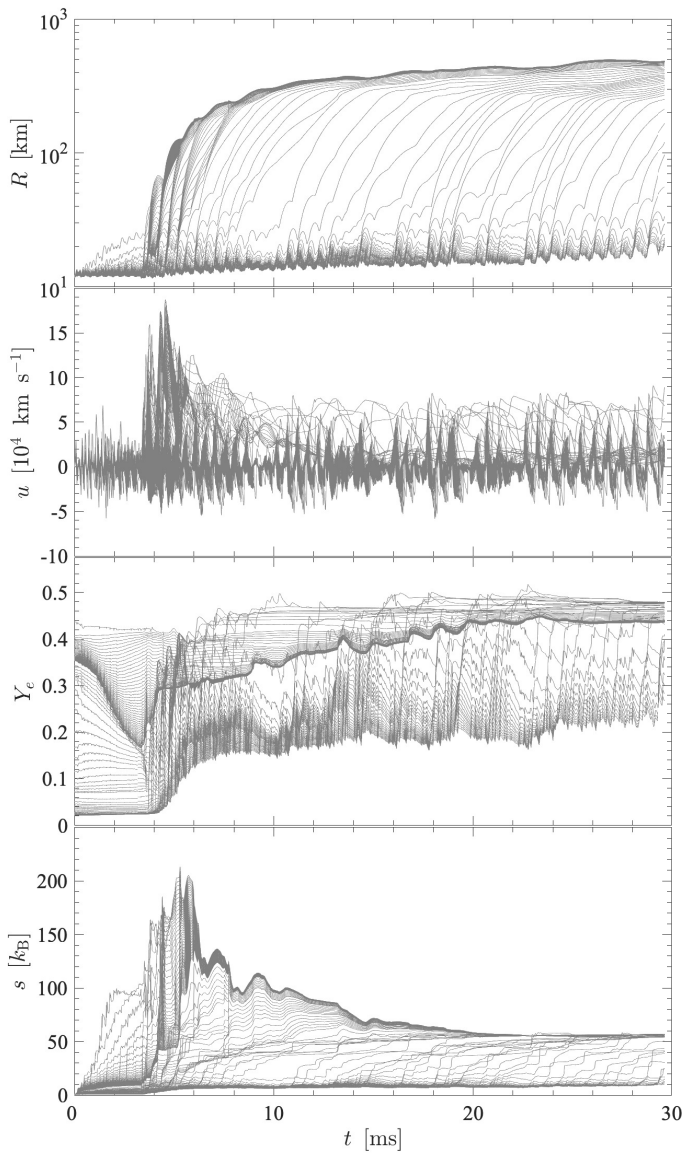


**Fig. 3.** Evolution of 230 selected baryonic mass shells corresponding to the material being ejected, showing the radius  $R$ , velocity  $u$ , electron fraction  $Y_e$  and restmass density  $\rho$ .

### 3. Neutron star simulations with phase transition

The initial conditions constructed in Sec. 2, corresponding to the NS with accreted envelope, are at the boundary between the hadronic phase and the onset conditions for the hadron-quark phase transition. In fact only the envelope mass of  $0.0181 M_\odot$  is above the mass onset. These solutions of the hydrostatic equations for  $s = 0.1 k_B$  are implemented into the neutrino radiation hydrodynamics model as initial conditions, considering the impact of the hadron-quark phase transition. In appendix A we confirm the hydrostatic equilibrium solution obtained within the hydrodynamics approach based on the DD2F EOS, implementing a high radial resolution of 300 mass mesh points.

Therefore, the spherically symmetric general relativistic neutrino radiation hydrodynamics model AGILE-BOLTZTRAN is employed. It was developed by Liebendörfer et al. (2004), see also Mezzacappa & Bruenn (1993c,a,b). It solves the neutrino radiation hydrody-

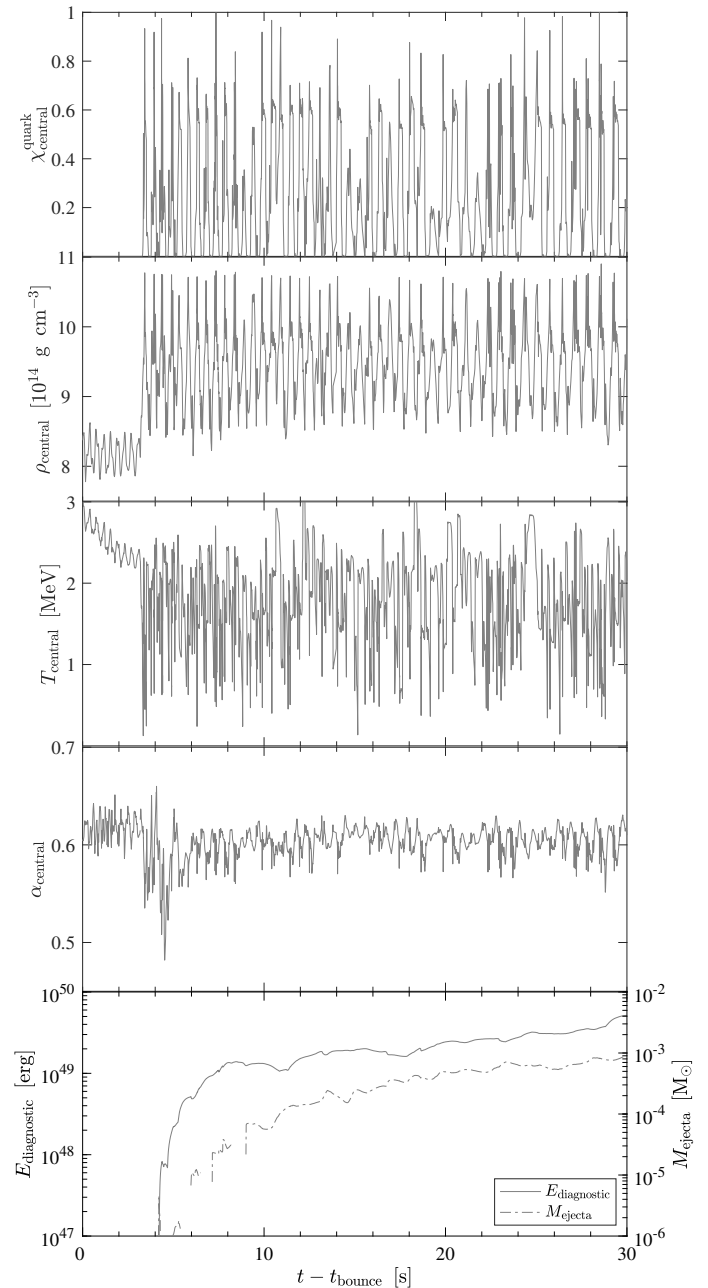


**Fig. 4.** Evolution of selected quantities, from top to bottom: central quark matter volume fraction  $\chi_{\text{central}}^{\text{quark}}$ , central restmass density  $\rho_{\text{central}}$ , central temperature  $T_{\text{central}}$ , central lapse function  $\alpha_{\text{central}}$ , and explosion energy estimate  $E_{\text{diagnostic}}$  as well as the ejected baryonic mass  $M_{\text{ejecta}}$ .

namics equations in co-moving coordinates (Liebendörfer et al., 2001), featuring an adaptive baryon mass mesh (see Liebendörfer et al., 2002; Fischer et al., 2009). The general relativistic three-flavor Boltzmann equation of Lindquist (1966) is solved for the transport of neutrinos. The collision integral includes the list of weak reactions considered here (see Table 1 of Fischer et al., 2020a), which includes the Urca processes including the (inverse) neutron decay within the full kinematics approach including weak magnetism contributions, following Guo et al. (2020), elastic neutrino nucleon/nucleus scattering following Bruenn (1985) with the approximate inclusion of inelastic

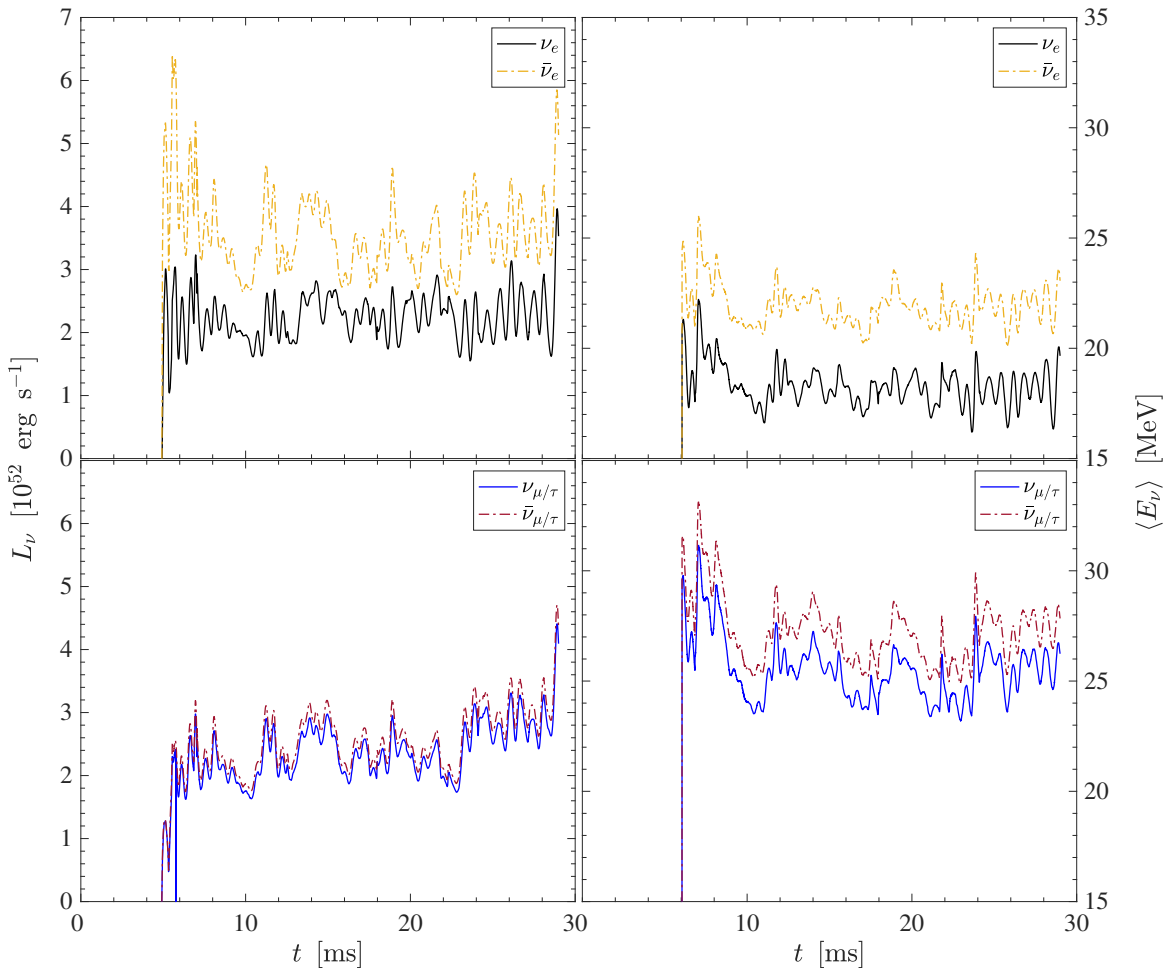


**Fig. 5.** Evolution of the neutrino luminosities (left panels) and average energies (right panels) for all flavors, sampled in the co-moving frame of reference at a radius of 200 km, for the DD2F-RDF-1.1 run.

contributions and weak magnetism following Horowitz (2002), inelastic neutrino electron/positron scattering of Mezzacappa & Bruenn (1993b) and neutrino pair processes. The latter consider electron/positron annihilation, nucleon-nucleon bremsstrahlung of Friman & Maxwell (1979) and Hannestad & Raffelt (1998), including  $\pi NN$  vertex corrections (see also Bartl et al., 2016; Guo & Martínez-Pinedo, 2019) implemented by Fischer (2016), and the annihilation of electron neutrino-antineutrino pairs to  $\mu/\tau$  neutrino-antineutrino pairs of Buras et al. (2006) implemented in Fischer et al. (2009).

The initial neutrino phase space distributions are set to zero at all neutrino energies and propagation angles, for all flavors. The time resolution is then adjusted to a very short scale, with timesteps on the order of sub-nanoseconds, to encompass all reaction rates, including the scattering and pair reaction kernels. This leads to the launch of an artificial startup neutrino burst, however, does not cause any impact on the evolution of the NS structure. It is also present in the reference hadronic run, discussed in Appendix A. The later neutrino evolution and impact of neutrino transport will be discussed below.

Figure 3 shows the evolution of 230 selected baryonic mass shells, between mass coordinates  $M = 1.776 M_\odot$  and  $M = 1.780676 M_\odot$ , which corresponds to the material being ejected in the simulations launched based on the DD2F-

RDF-1.1 hybrid EOS. After an initial period during which the accreted envelope expands slightly, as a direct response to the thermal pressure in the radiation dominated low-density domain, the central quark matter fraction, denoted as  $\chi^{\text{quark}}$ , rises slowly, as illustrated in the top panel of Fig. 4 after about 3 ms, however, never reaching and remaining in the pure quark matter phase. The latter is defined as  $\chi^{\text{quark}} = 1$ , where  $\chi^{\text{quark}} = 0$  corresponds to matter being in the hadronic phase and in the hadron-quark mixed phase  $0 < \chi^{\text{quark}} < 1$  (further details about the definitions of  $\chi^{\text{quark}}$  can be found in Bastian, 2021). The matter velocities, shown in Fig. 3, oscillate accordingly on the order of a few times  $10^4 \text{ km s}^{-1}$  reaching in the peaks  $1.5 \times 10^5 \text{ km s}^{-1}$ .

After the softening of the central NS EOS, due to the onset of the phase transition—note that the hybrid EOS softens significantly in the hadron-quark mixed phase where the pressure slope decreases (see Fig. 1)—the central density rises rapidly. It oscillates in accordance with the central quark matter fraction around a mean value of about  $10^{15} \text{ g cm}^{-3}$ , as is illustrated in the top panel of Fig. 4. The onset of the phase transition at the NS interior is accompanied by a decreasing central temperature, as shown in Fig. 4. This phenomenon is known for this class of RDF hybrid EOS, i.e. during the adiabatic compression of the central NS fluid elements, the temperature decreases. It has been discussed at the example of core-collapse supernovae

in Fischer et al. (2018) and Fischer (2021). In the hadron-quark mixed phase, after around 3 ms, the temperature of the central fluid elements oscillate accordingly, though on a larger magnitude than before reaching the mixed phase, similar to the central temperatures, due to the substantially larger EOS gradients encountered in the mixed phase.

As a consequence of the evolution after reaching quark matter at the neutron star interior, the steeper gravitational potential results in increased temperatures at the neutron star surface where the accreted envelope expands, reaching supersonic matter velocities. This rapid initial expansion is illustrated in Fig. 3 (top panel). The entire envelope expands quickly to radii on the order of several 100 km. At about 15 ms, the outer envelope reaches a radius of about 400 km. This evolution is accompanied by the constant change of the gravitational potential, illustrated via the central lapse function  $\alpha_{\text{central}}$  in Fig. 4 dropping from 0.62 to slightly below 0.5, and hence oscillations of the neutron star surface, which in turn, affects the central evolution as shown in Fig. 4. The associated millisecond timescale of these oscillations is related to the high central densities on the order of  $10^{15} \text{ g cm}^{-3}$  and the CFL conditions for the numerical scheme solving the system of a partial differential equation, i.e. the time resolution decreases by a factor of 2 when the density increases from  $\rho = 10^{14} \text{ g cm}^{-3}$  to  $\rho = 10^{15} \text{ g cm}^{-3}$ .

At the moment of the hadron-quark phase transition, when the NS envelope expands, positive diagnostic explosion energies are obtained. These are evaluated by integrating the total energy, composed of gravitational, kinetic, and internal energies, the latter given by the EOS, from the surface towards the center, following thereby the standard procedure of core-collapse supernova phenomenology (c.f. Fischer et al., 2009, and references therein). Values of about  $E_{\text{diagnostic}} \simeq 5 \times 10^{49} \text{ erg}$  are obtained at about 30 ms of simulation time, as illustrated in Fig. 4 (bottom panel), however, still the asymptotic value has not been reached yet. The total mass ejected is about  $M_{\text{ejecta}} \simeq 1 \times 10^{-3} M_{\odot}$ , for the simulation time. These ejecta feature high escape velocities, on the order of 10–60% of the speed of light (see Fig. 3).

It is interesting to note that these ejecta are subject to neutrino interactions as they expand, which give rise to a broad  $Y_e$  distribution (see Fig. 3). There is an early component featuring slightly neutron-rich conditions with  $Y_e \simeq 0.3 - 0.45$  and high entropies per baryon on the order of  $s \simeq 100 - 175 k_B$  as illustrated in the bottom panel of Fig. 3. It is followed by an isospin symmetric component with  $Y_e \simeq 0.5$  and moderately low entropies per baryon of  $s \simeq 50 k_B$ . The neutrino luminosities and average energies are shown in Fig. 5 for all flavors, sampled in the co-moving reference frame at a radius of 200 km. This corresponds to the free-streaming regime. Luminosities rise suddenly after about 6 ms, coinciding when quark matter appears at the NS interior, reaching values of a few times  $10^{52} \text{ erg s}^{-1}$  with average energies on the order of several tens of MeV. Initially, i.e. before the appearance of quark matter, the neutrino luminosities are on the order of  $10^{49} \text{ erg s}^{-1}$  and the average energies are on the order of few MeV, as is discussed and illustrated in Appendix A. Note further, the reason for the early ejecta to remain low  $Y_e$  is due to the high expansion velocities on the order of 60% of the speed of light, while for the later ejecta the neutrino fluxes and their average energies are responsible for the rising  $Y_e$ , similar as

has been found semi-analytically for the late-time supernova ejecta by Qian & Woosley (1996). Since the spectral and flux differences remain generally small, in particular, the difference  $\langle E_{\bar{\nu}_e} \rangle - \langle E_{\nu_e} \rangle$  remains small, on the order of few MeV, despite the generally high average energies on the order of 15–25 MeV for both  $\nu_e$  and  $\bar{\nu}_e$ , the spectral difference is insufficient to keep the expanding material neutron-rich.

#### 4. Mode analysis

In this section results of an in-depth mode analysis are conducted following the approach of Torres-Forné et al. (2019b) employing the numerical GREAT code. It solves the eigenvalue problem of hydrodynamic and metric perturbations of a spherically symmetric self-gravitating system equilibrium model in General Relativity. Assuming spherical symmetry, these eigenmodes are obtained through linear adiabatic perturbation analysis of the hydrodynamics and metric equations with a background in equilibrium. This linear Eulerian perturbation is expanded with a harmonic time dependence of frequency and in spherical harmonics for the angular dependence (see Torres-Forné et al., 2019b). The corresponding Lagrangian fluid element displacement vector can then be expressed as follows,

$$\boldsymbol{\xi} = \left[ \eta_r(r) Y_{lm}(\theta, \varphi) \hat{\mathbf{r}} + \eta_{\perp}(r) \left( \frac{\partial_{\theta} Y_{lm}(\theta, \varphi)}{r^2} \hat{\boldsymbol{\theta}} + \frac{\partial_{\varphi} Y_{lm}(\theta, \varphi)}{r^2 \sin^2 \theta} \hat{\boldsymbol{\phi}} \right) \right] e^{i\sigma t} \quad (1)$$

where we use spherical coordinates  $(r, \theta, \varphi)$  with its corresponding orthonormal basis  $(\hat{\mathbf{r}}, \hat{\boldsymbol{\theta}}, \hat{\boldsymbol{\phi}})$  and the spherical harmonics  $Y_{lm}$ . Here,  $\sigma$  is the oscillation frequency in the harmonic time-dependent part.  $\eta_r$  and  $\eta_{\perp}$  are two functions of the radius that characterize the radial and angular components of the displacement, respectively.

Employing the relativistic Brunt-Väisälä frequency and the relativistic Lamb frequency, denoted as  $N^2$  and  $L^2$ , respectively (see Eqs. (33) and (34) in Torres-Forné et al., 2018), is a valuable approach to identify regions of possible convection. The former is related to the criterion of Ledoux stability and quantified by the presence of lepton number and entropy gradients (c.f. Mirizzi et al., 2016, and references therein). In general,  $N^2$  governs gravity ( $g$ ) modes and  $L^2$  dictates pressure ( $p$ ) modes and the fundamental ( $f$ ) mode.

Distinct modes can emerge contingent upon the temporal evolution of diverse physical parameters. Gravity modes manifest in regions where buoyancy serves as a restoring force, characterized by  $N^2 > 0$ , indicating stability to convective motion. In the absence of buoyancy,  $p$  modes are excited by the propagation of sound waves. Our focus lies not in the modes supported by sound waves, but rather in the interior of the NS. Although the NS is not fully isolated, and the choice of boundary conditions influences  $p$ -mode eigenfrequency calculations, our attention is directed solely toward the NS interior. We impose boundary conditions from the innermost fluid elements to the surface of the NS. It is crucial to note that the definition of the NS surface is based on the density profile reaching  $\rho = 10^{11} \text{ g cm}^{-3}$ . The inner boundary is set to be the central fluid element. Altering the inner boundary to somewhat lower densities,

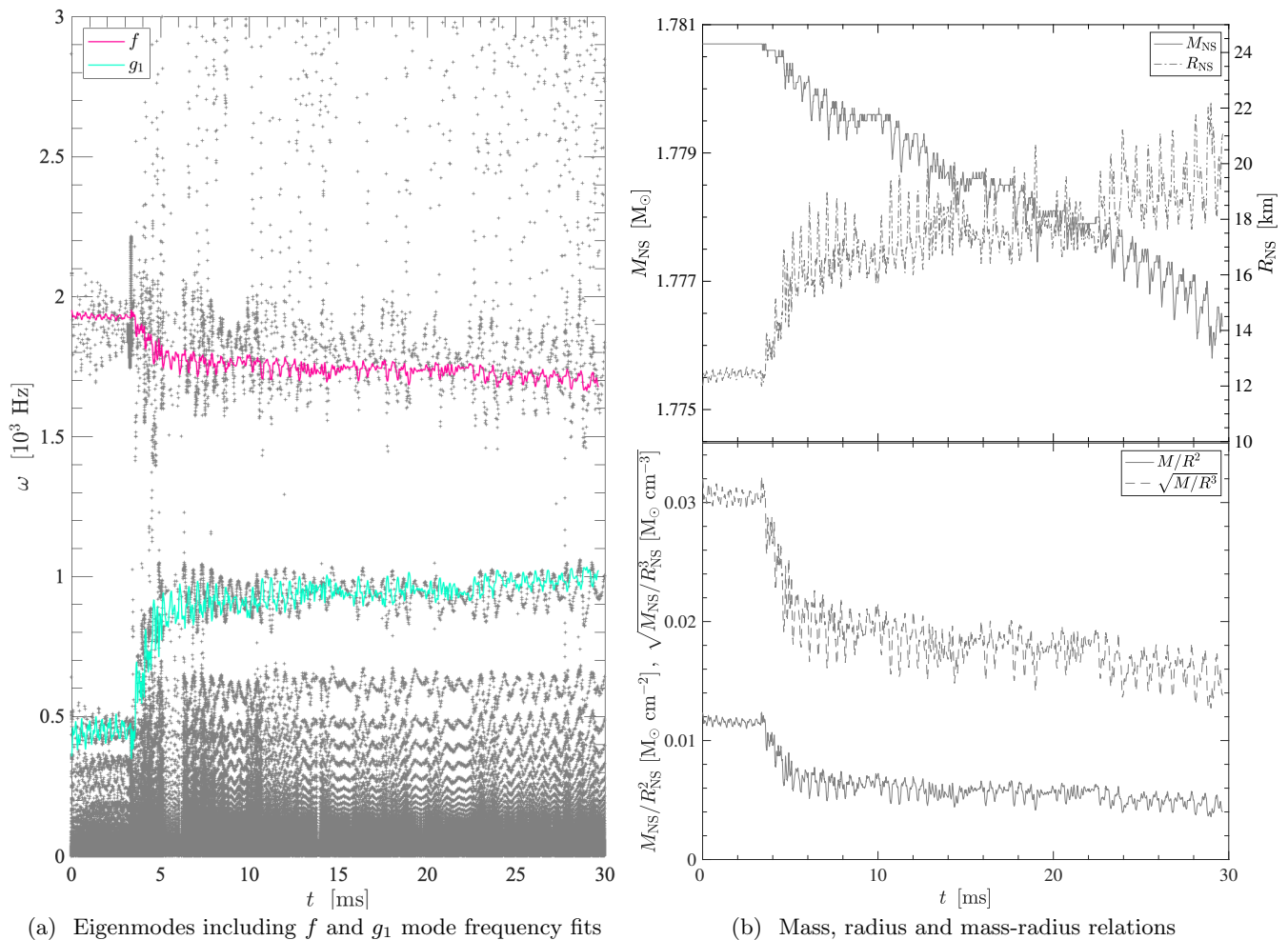


**Fig. 6.** Results of the mode analysis (left panel), showing the solutions of the GREAT analysis (black dots) and the fit expression (2) for the dominant mode (solid purple line), see text for details, as well as the corresponding evolution of the NS (right panel), enclosed mass  $M_{\text{NS}}$  and radius  $R_{\text{NS}}$ , sampled at a restmass density of  $\rho = 10^{11} \text{ g cm}^{-3}$ .

e.g.,  $\rho = 10^{14} \text{ g cm}^{-3}$ , has a negligible impact on the solutions, given the lack of significant density fluctuations within the NS inner core.

The frequency outcomes derived from mode analysis via the GREAT tool are depicted in the left panel of Fig. 6. These results encompass solutions obtained for all nodes with  $l = 2$ , spanning the frequency range of 0 to 4 kHz. Due to the chosen boundary conditions, the majority of modes associated with  $p$  modes fall beyond this range. Following the mode classification of Cowling (1941), the foremost dominant mode, characterized by zero nodes and identified as the  $f$  mode, initiates at approximately 1.9 kHz. Subsequently, reaching the onset density for the first-order QCD phase transition, it experiences a slight reduction and transiently follows a descending trajectory. At lower frequencies, another prominent mode with  $n = 1$  node emerges as the first  $g$  mode, with a broader frequency spectrum compared to the  $f$  mode and distinctive behavior. It commences at approximately 0.5 kHz and exhibits a sudden, drastic rise to frequencies around 1 kHz after reaching the onset density for the QCD phase transition. Despite the neutron star never fully reaching a quark matter core and

undergoing oscillations in mass and radius, the  $g$ -mode, on the whole, evolves toward higher frequencies.

In accordance with the node definition proposed by Torres-Forné et al. (2018), the quantity  $n$  is herein defined as the count of sign changes within the radial function  $\eta_r$ . These are shown in Fig 7 at three different times, corresponding to the hadronic evolution before the appearance of quark matter (left panel), during the transition when quark matter appeared at the NS interior (middle panel) and during the long-term evolution after (right panel). The associated frequencies are listed in the legend, coinciding with the definition of Torres-Forné et al. (2018), confirming the highest frequency mode as  $f$  mode and the other two lower frequencies as  $g$  modes. Radial profiles of both,  $N$  and  $L$  frequencies, are shown in Fig. 7 in the panels below. Note that the plane-wave approximation imposes the condition,  $L^2 > N^2$ , for acceptable solutions. In other words, oscillatory solutions can occur when  $\sigma^2 > N^2, L^2$  (representing acoustic waves), or when  $\sigma^2 < N^2, L^2$  (indicating gravity waves). Intermediate values lead to non-oscillatory evanescent solutions. It is essential to acknowledge that this simplifying assumption may not be applicable in the present context. The NS system features finite entropy, potentially



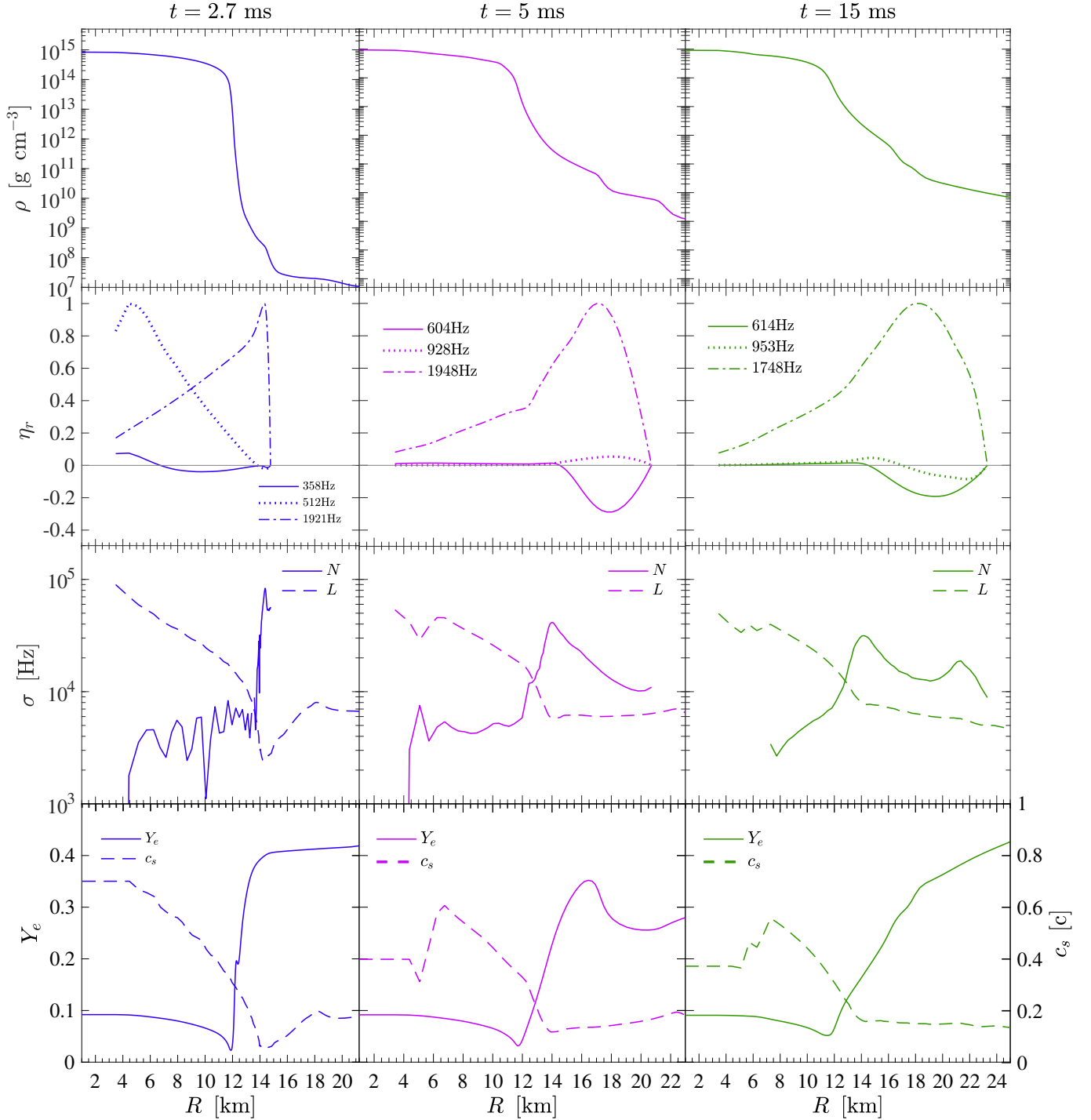


**Fig. 7.** Radial profiles of selected quantities, from top to bottom, showing restmass density  $\rho$ , radial solutions of the eigenfrequencies  $\eta_r$  for the highest three modes found, indicating the corresponding frequencies, further the Lamb  $L$  and Brunt-Väisälä  $N$  frequencies as well as  $Y_e$  and speed of sound  $c_s$ , at three different times (see Fig. 6), corresponding to the hadronic evolution in graph (a), the transition when quark matter appears in graph (b) and at late times in graph (c).

deviating from the conditions under which this approximation is valid. In particular, it becomes evident from Fig. 7, that the rise of  $N^2$  is dominated by the presence of a large lepton number gradients, indicated by the rising  $Y_e$  profile at radii above around 12 km, since lepton number and entropy gradients at the NS interior are negligible as, in particular, the initial conditions assume constant entropy per particle at the NS interior. Entropy fluctuations remain

overall small during the entire simulation and the speed of sound,  $c_s$ , shown in the bottom panel of Fig. 7 is small,  $(c_s/c)^2 \simeq 0.1\text{--}0.3$ , and nearly constant towards larger radii. At the interior, however, the value of the speed of sound exceeds the perturbative QCD limit of  $(c_s/c)^2 = 1/3$ , since the conditions correspond to the highly non-perturbative regime of QCD. Note further the evolution of the  $f$  and  $g_1$  frequencies via the associated radial solutions  $\eta_r$  in Fig. 7,

which quantifies the results shown in Fig. 6 at the three selected times.

**Table 1.** Parameters for the frequency fits expression (2).

mode	$x$	$a_0$	$a_1$	$a_2$
$f$	$\sqrt{M_{\text{NS}}/R_{\text{NS}}^3}$	1470	$1.5 \times 10^4$	0
$g_1$	$M_{\text{NS}}/R_{\text{NS}}^2$	1075	$8 \times 10^3$	$-5.4 \times 10^6$

In order to fit the frequency results to the evolution of NS bulk properties, such as the enclosed mass and its radius, we closely follow the discussion in Torres-Forné et al. (2019a), and express linear and quadratic frequency fits for the dominant and the first sub-dominant modes, respectively, in terms of the mean density inside the NS,  $x \equiv \sqrt{M_{\text{NS}}/R_{\text{NS}}^3}$ , and in terms of surface gravity,  $x \equiv M_{\text{NS}}/R_{\text{NS}}^2$ , as follows:

$$\omega_{\text{fit}}(x) = a_0 + a_1 x + a_2 x^2, \quad (2)$$

with the fit parameters  $a_0$ ,  $a_1$  and  $a_2$  are given in Table 1 for the dominant and the first sub-dominant modes identified. This indicates that the frequency fits found, the dominant one initially at around 2 kHz and descending towards 1.6 kHz after the phase transition is an  $f$  mode, and the one starting at around 500 Hz and the rapidly rising frequency to about 1000 Hz, is the  $g_1$  mode, the magenta and turquoise lines, respectively. The corresponding evolution of the enclosed NS mass and radius are shown in the right panel of Fig. 6, sampled at a restmass density of  $\rho = 10^{11} \text{ g cm}^{-3}$ , to avoid  $p$  modes. The general tendency, i.e. the ratio of  $M/R$  decreases after the appearance of quark matter at the NS interior, is due to the ejection of material from the NS surface as a consequence of the dynamical response of the system to the central NS oscillations discussed in sec. 3. All other sub-dominant modes are higher  $g_l$ -modes.

## 5. Summary and conclusions

The present paper discusses NS in accreting systems as a novel astrophysical scenario for the appearance of QCD degrees of freedom. To this end, general relativistic neutrino radiation hydrodynamics simulations are performed based on three flavor Boltzmann neutrino transport in spherical symmetry. Initial conditions are constructed based on the well selected DD2F nuclear EOS for a NS with a total baryonic mass of  $1.781 M_{\odot}$ , featuring an accreted envelope of  $M_{\text{envelope}} = 0.018 M_{\odot}$ , corresponding to the hybrid branch of the mass-radius relation of the DD2F-RDF-1.1 hybrid EOS employed in this study. It features a first-order phase transition based on the Maxwell construction from the DD2F RMF nuclear matter EOS to the RDF-1.1. model. The latter includes vector repulsion which is responsible for the stiffening of the EOS with increasing density and hence yielding maximum hybrid star masses, which are consistent with the current constraint of about  $2 M_{\odot}$ . The appearance of quark matter at the NS interior causes the NS's central density to rapidly rise and oscillate on a timescale on the order of milliseconds. In response to the central contraction, matter is expelled from the hybrid star's surface, resulting in the ejection of approximately  $10^{-3} M_{\odot}$  of baryonic mass

during the considered simulation times. Explosion energy estimates are obtained of  $5 \times 10^{49} \text{ erg}$ , computed following the procedure commonly used in the core-collapse supernova context.

Due to the sudden compression and later, long-term oscillations of the hybrid star interior, that lasts at least for several tens of milliseconds, the hybrid star experiences a temperature increase, in particular at low densities towards the surface. This, in turn, results in the production of neutrinos with luminosities on the order of  $10^{52} \text{ erg s}^{-1}$  and average energies of several tens of MeV. This represents an observable signal for the current generation of kiloton water-Cherenkov radiation detectors for a galactic event.

The Urca processes, electron captures on protons and positron capture on neutrons, as well as their reverse  $\nu_e$  and  $\bar{\nu}_e$  captures, and the (inverse)neutron decay, cause the rise of the  $Y_e$  of the ejected material, from  $Y_e \leq 0.46$  to  $Y_e \simeq 0.5$ . However, the release of a millisecond burst-like neutrino signature, as was reported for the QCD phase transition in the context of core-collapse supernovae (c.f. Fischer et al., 2018, and references therein), has not been found here. On the other hand, a detailed GW mode analysis shows the evolution of the decreasing dominant  $f$ -mode frequency from around 1.9 kHz, in the hadronic phase, towards around 1.7 kHz, after the appearance of quark matter. The magnitude of the decrease reported here for the particular NS mass is consistent with the findings of Sotani & Kojo (2023), who further studied a range of compact stars between  $1.0$ – $2.3 M_{\odot}$  comparing models with QCD degrees of freedom to a reference hadronic case, finding the increase of the decreasing  $f$ -mode frequencies for more massive stars. The present study reports in addition about the  $g_1$  mode evolution, for which we find a sudden rise from 0.5 kHz, in the hadronic phase, to about 1 kHz after the appearance of quark matter. The lower  $g_l$ -mode frequencies, i.e.  $l \geq 2$ , follow qualitatively the behaviour of  $g_1$ . We provide linear and quadratic fits of the  $f$ - and  $g_1$ -mode frequencies, following the argumentation of Torres-Forné et al. (2019a), in terms of the mean density and surface gravity, respectively.

It is interesting to note that a complete phase transition, i.e. the central NS reaches and stays in the pure quark matter, was not found, even though the initial conditions belong to the hybrid branch of the mass-radius relation, by an amount of exactly  $M_{\text{envelope}}$ . Mass transfer in binary systems—from a main sequence star to a secondary NS—results in the slow accumulation of material at the NS surface and hence the growth of the NS total mass. A low-mass NS born in a core-collapse supernova explosion without QCD phase transition will slowly move along the mass-radius relation towards increasing mass. The present investigation demonstrates quantitatively, for a particular hadron-quark hybrid EOS, the hydrodynamical evolution when such system reaches the conditions for the onset of the QCD phase transition. It remains to be explored what is the role of the EOS, in terms of varying onset densities for quark matter as well as bulk properties of the phase transition such as the pressure slope and other dependencies of the hadron-quark mixed phase, such as the possible presence of shear (Sotani et al., 2013) and associated presence of geometric structures collectively known as 'Pasta' phases (c.f. Yasutake et al., 2014, and references therein), which we leave for future exploration.

Furthermore, the impact of potentially high magnetic fields and rapid rotation, associated with the very existence of magnetars, require the multi-dimensional magneto neutrino radiation hydrodynamics framework. The present work is limited to NS with low surface magnetic fields, referring to old NS. However, the response of the system reported here due to the QCD phase transition is expected to remain qualitatively, independent of the magnetic field, featuring the ejection of material from the NS surface and the rise of the neutrino fluxes to observable values as well as the emission of GW with kHz frequencies. The magnitude of the frequencies might alter as well as the amount of mass ejected as the oscillations reported here will be damped by the emission of GW in multi-dimensional simulations, as was demonstrated in the multi-dimensional hydrodynamics simulations of [Dimmelmeier et al. \(2009\)](#), based on polytropic parametrised and MIT bag model EOS, settling the NS back into the initial stable state on a longer timescale.

## Acknowledgements

The authors (N.K.L., T.F., and S.S.) acknowledge support from the Polish National Science Centre (NCN) under grant number 2020/37/B/ST9/00691. P.C.D and A.T.F acknowledge support from the Spanish Agencia Estatal de Investigación (Grants No. PGC2018-095984-B-I00 and PID2021-125485NB-C21) funded by MCIN/AEI/10.13039/501100011033 and ERDF A way of making Europe, by the Generalitat Valenciana (PROMETEO/2019/071), and by COST Actions CA16104 and CA16214.

## ORCID iDs

Noshad Khosravi Largani <https://orcid.org/0000-0003-1551-0508>

Tobias Fischer <https://orcid.org/0000-0003-2479-344X>

Shota Shibagaki <https://orcid.org/0000-0002-8196-0745>

Pablo Cerdá-Durán <https://orcid.org/0000-0001-7354-6897>

Alejandro Torres-Forné <https://orcid.org/0000-0001-8709-5118>

## Appendix A: Hydrostatic equilibrium solution

To quantify hydrostatic equilibrium, neutrino radiation hydrodynamics simulations are launched for the reference DD2F hadronic EOS, featuring a high radial resolution of 300 radial mass shells implemented in `AGILE-BOLTZTRAN`. Otherwise, the same input physics is used as discussed in Sec. 3. After an initial relaxation phase lasts for about 5–10 ms, the central compact NS settles into complete hydrostatic equilibrium. The results are illustrated in Fig. A.1 for all 300 mass shells, showing the evolution of selected quantities (from top to bottom), radius, velocity, restmass density, temperature and  $Y_e$ . The evolution of all central mass shells remains constant values for all quantities, corresponding to the neutron star interior for densities as low as  $\rho \simeq 10^6 \text{ g cm}^{-3}$ . The accreted envelope, on the other hand, does not obey complete hydrostatic equilibrium, illustrated via expanding and contracting mass shells, up to radii of about 40 km and the velocities correspondingly reach values of a few times  $10^4 \text{ km/s}$ . Densities and temperatures

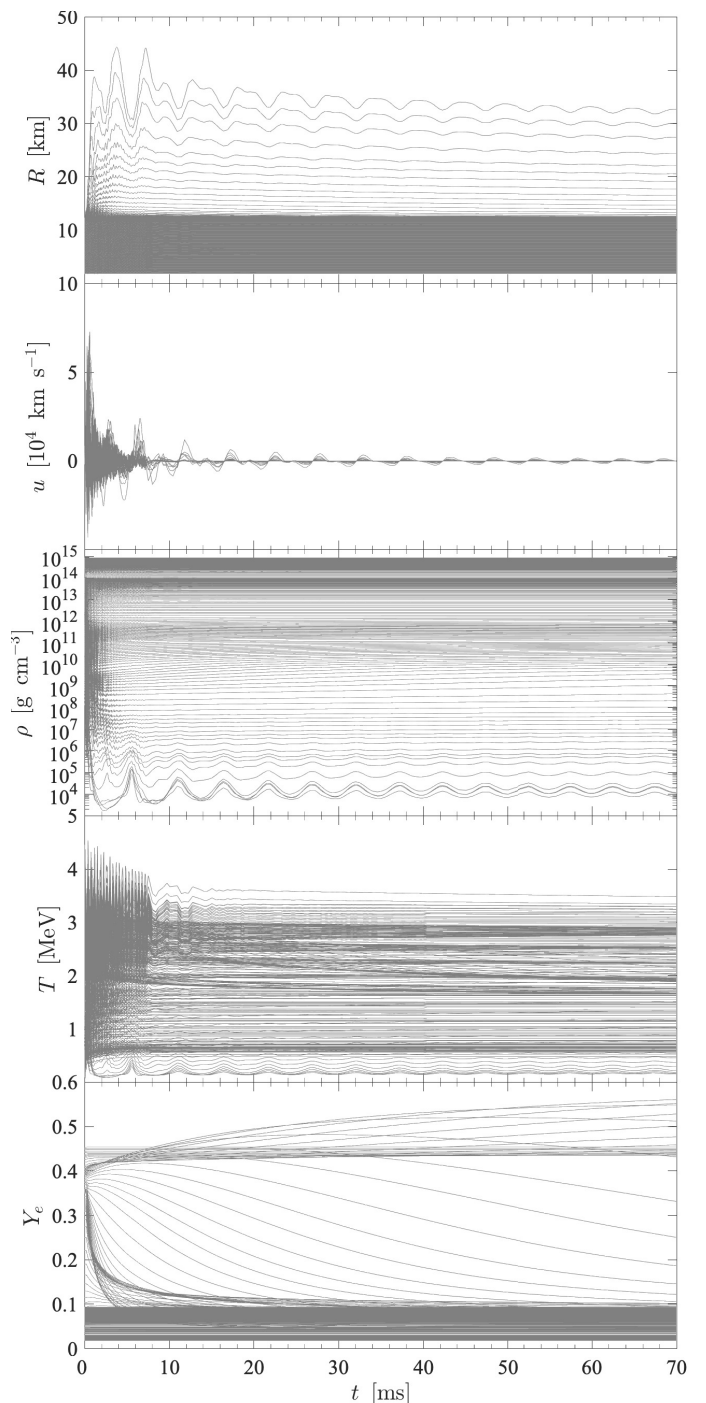


**Fig. A.1.** Evolution of mass shells for the reference DD2F hadronic model, showing the evolution of (from top to bottom) radius, velocity, restmass density, temperature and electron fraction.

follow accordingly, oscillating around  $\rho \simeq 10^4 \text{ g cm}^{-3}$  and  $T \simeq 0.2 \text{ MeV}$ . The oscillations are damped towards later times on the order of several tens of milliseconds.

All matter remains gravitationally bound at all times during the simulation and hence no positive explosion energy estimate is obtained. The situation is illustrated via radial profiles of selected quantities in Fig. A.2, comparing the initial conditions (thick grey lines) and at about 38 ms of simulation time (thin red lines), showing the expansion

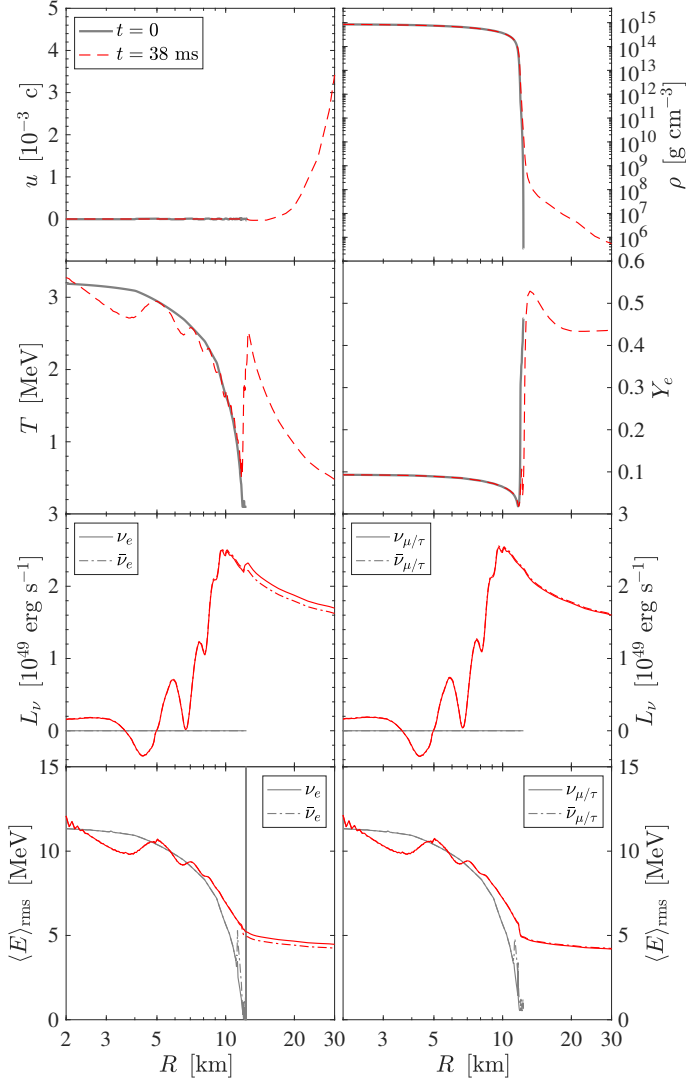


**Fig. A.2.** Radial profiles of selected quantities, velocity  $u$  in units of the speed of light  $c$ , restmass density  $\rho$ , temperature  $T$ , electron abundance  $Y_e$ , and neutrino luminosities  $L_\nu$  and root mean square energies  $\langle E \rangle_{\text{rms}}$  of all flavors, comparing the reference DD2F hadronic simulation at  $t = 0$  and  $t \simeq 38$  ms of simulation time.

of the envelope to radii of about 100 km and the subsequent density, temperature and  $Y_e$  profiles.

The evolution of the neutrino luminosities and average energies are shown in Fig. A.3 for all flavors. The values of the luminosities remain generally low, on the order of a few  $10^{49}$  erg  $s^{-1}$ , with average energies of  $\langle E_\nu \rangle \simeq 4$  MeV, after the initial relaxation phase of about 10 ms. The neutrinos stem from the neutron star’s surface, where the neutrino luminosities rise. Values of the neutrinosphere radii,  $R_\nu$ , are given in Fig. A.4, following the standard definition via the optical depth  $\tau_\nu$ , where  $R_\nu := r(\tau_\nu \equiv 2/3)$ , which settle towards constant values between  $R_{\nu_{\mu/\tau}} \simeq 10.75$  km,  $R_{\nu_e} \simeq 10.81$  and  $R_{\bar{\nu}_e} = 10.85$  after the initial relaxation period. The radial profile of the luminosities and root-mean-square energies  $\langle E \rangle_{\text{rms}}$  are illustrated in the bottom panels of Fig. A.2, which is the transition between neutron star crust and previously accreted envelope, corresponding to the sharp rise of the envelope temperature.

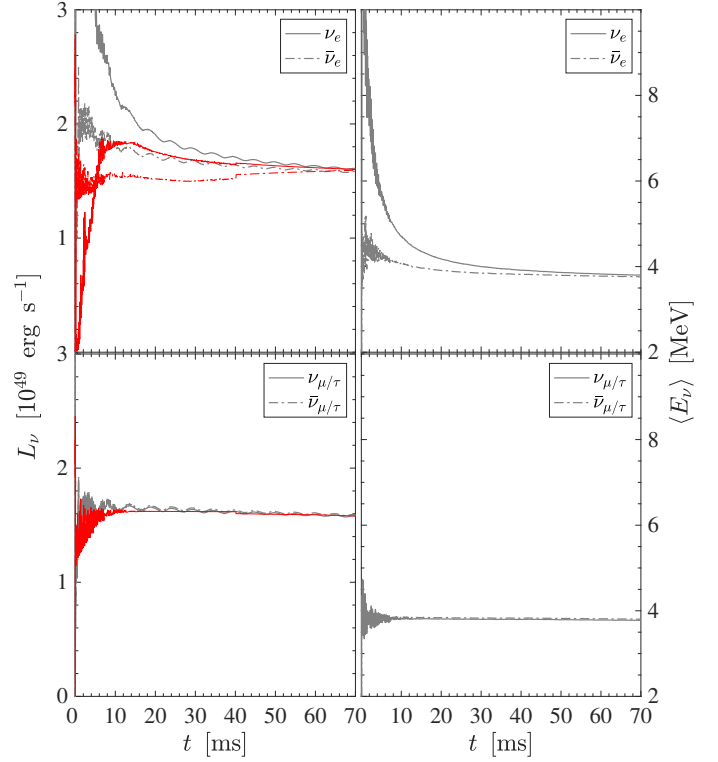


**Fig. A.3.** Evolution of neutrino luminosities (left panels) and average energies (right panels) for all  $\nu_e$  and  $\bar{\nu}_e$  (top panels) and heavy lepton flavors (bottom panels), for the DD2F hadronic reference simulations (grey lines), in comparison to the diffusion approximation (red lines) following Expression (A.1).

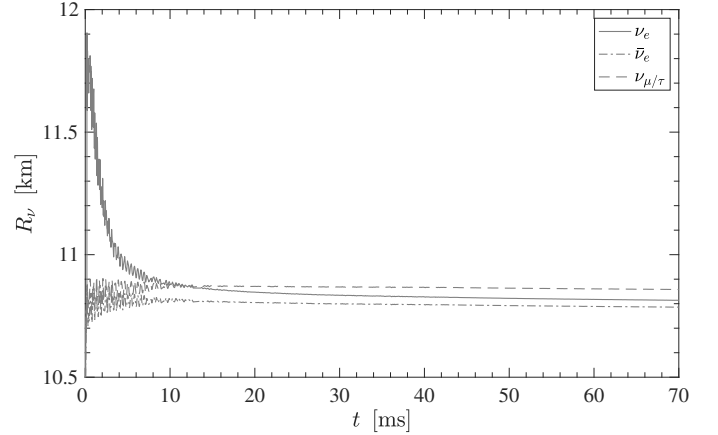


**Fig. A.4.** Evolution of the neutrinospheres  $R_\nu$  of all flavors.

The Urca processes drive the electron abundance of the expanding envelope from initially  $Y_e \simeq 0.46$  towards  $Y_e \simeq 0.5$ , and even above at later times, as shown in Fig. A.2. The increasing  $Y_e$  of the crust-envelope interface is also shown in the evolution of the mass shells in the bottom panel of Fig. A.1. This is the reason for the hierarchy of the neutrino luminosities,  $L_{\nu_e} \gtrsim L_{\bar{\nu}_e}$ , and average energies,  $\langle E_{\nu_e} \rangle \gtrsim \langle E_{\bar{\nu}_e} \rangle$ , however, comparable to other weak processes, which is the cause for the heavy lepton flavor neutrino luminosities and average energies being of similar order as those of the electron flavors. Note that the neutrino

luminosities approach asymptotically the diffusion limit,

$$L_T \simeq 4\pi\sigma_{\text{SB}} \kappa_\nu R_\nu^2 T_\nu^4, \quad (\text{A.1})$$

where  $\kappa_\nu$  is an empirical factor that is of order 20%; 1/6 for  $\nu_e$ , 10/52 for  $\bar{\nu}_e$  and 10/46 for the heavy lepton neutrino flavors. The values of the neutrino luminosities (A.1) are shown in Fig. A.3 as red lines, for comparison. This approximation has been explored in the core-collapse supernova case for both the fail branch in Fischer et al. (2009) as well as for the proto-neutron star deleptonization and later cooling phases in Fischer et al. (2012). Here, particularly during the early evolution, (A.1) particularly reproduced the behavior of the heavy lepton neutrino flavor. The evolution of the neutrinospheres of the last scattering is shown in Fig. A.4 for which the method based on the integration of the transport mean free path of Fischer et al. (2012) has been employed.

## References

- Abbott, B. P., Abbott, R., Abbott, T. D., et al. 2018, *Phys. Rev. Lett.*, 121, 161101
- Alpar, M. A., Langer, S. A., & Sauls, J. A. 1984, *ApJ*, 282, 533
- Anderson, P. W. & Itoh, N. 1975, *Nature*, 256, 25
- Andersson, N., Ferrari, V., Jones, D. I., et al. 2011, *General Relativity and Gravitation*, 43, 409
- Andersson, N. & Kokkotas, K. D. 1998, *MNRAS*, 299, 1059
- Annala, E., Gorda, T., Kurkela, A., Nättilä, J., & Vuorinen, A. 2020, *Nature Physics*, 16, 907
- Antoniadis, J., Freire, P. C. C., Wex, N., et al. 2013, *Science*, 340, 448
- Bartl, A., Bollig, R., Janka, H. T., & Schwenk, A. 2016, *Phys. Rev. D*, 94, 083009
- Bastian, N.-U. F. 2021, *Phys. Rev. D*, 103, 023001
- Bastian, N.-U. F., Huovinen, P., & Nazarova, E. 2023, *Nucl. Phys. A*, 1038, 122718
- Bauswein, A., Bastian, N.-U. F., Blaschke, D. B., et al. 2019, *Phys. Rev. Lett.*, 122, 061102
- Bazavov, A., Ding, H. T., Hegde, P., et al. 2019, *Physics Letters B*, 795, 15
- Benhar, O., Ferrari, V., & Gualtieri, L. 2004, *Phys. Rev. D*, 70, 124015
- Benić, S., Blaschke, D., Alvarez-Castillo, D. E., Fischer, T., & Typel, S. 2015, *A&A*, 577, A40
- Bilous, A. V., Watts, A. L., Harding, A. K., et al. 2019, *ApJ*, 887, L23
- Blackler, S., Bastian, N.-U. F., Bauswein, A., et al. 2020, *Phys. Rev. D*, 102, 123023
- Bonazzola, S. & Gourgoulhon, E. 1996, *A&A*, 312, 675
- Bruenn, S. W. 1985, *ApJS*, 58, 771
- Buras, R., Janka, H.-T., Rampp, M., & Kifonidis, K. 2006, *A&A*, 457, 281
- Cerdá-Durán, P., DeBrye, N., Aloy, M. A., Font, J. A., & Obergaulinger, M. 2013, *ApJ*, 779, L18
- Chamel, N. & Haensel, P. 2008, *Living Reviews in Relativity*, 11, 10
- Chomiuk, L., Metzger, B. D., & Shen, K. J. 2021, *ARA&A*, 59, 391
- Cowling, T. G. 1941, *MNRAS*, 101, 367
- Danielewicz, P., Lacey, R., & Lynch, W. G. 2002, *Science*, 298, 1592
- De, S., Finstad, D., Lattimer, J. M., et al. 2018, *Phys. Rev. Lett.*, 121, 091102
- Dimmelmeier, H., Bejger, M., Haensel, P., & Zdunik, J. L. 2009, *MNRAS*, 396, 2269
- Eldridge, J. J. 2017, in *Handbook of Supernovae*, ed. A. W. Alsabti & P. Murdin, 671
- Espinoza, C. M., Lyne, A. G., Stappers, B. W., & Kramer, M. 2011, *MNRAS*, 414, 1679
- Fischer, T. 2016, *A&A*, 593, A103
- Fischer, T. 2021, *EuPhJA*, 57, 270
- Fischer, T., Bastian, N.-U., Blaschke, D., et al. 2017, *PASA*, 34, e067
- Fischer, T., Bastian, N.-U. F., Wu, M.-R., et al. 2018, *Nature Astronomy*, 2, 980
- Fischer, T., Guo, G., Dzhioev, A. A., et al. 2020a, *Phys. Rev. C*, 101, 025804
- Fischer, T., Martínez-Pinedo, G., Hempel, M., & Liebendörfer, M. 2012, *Phys. Rev. D*, 85, 083003
- Fischer, T., Sagert, I., Pagliara, G., et al. 2011, *ApJS*, 194, 39
- Fischer, T., Typel, S., Röpke, G., Bastian, N.-U. F., & Martínez-Pinedo, G. 2020b, *Phys. Rev. C*, 102, 055807
- Fischer, T., Whitehouse, S. C., Mezzacappa, A., Thielemann, F.-K., & Liebendörfer, M. 2009, *A&A*, 499, 1
- Fonseca, E., Cromartie, H. T., Pennucci, T. T., et al. 2021, *ApJ*, 915, L12
- Friman, B. L. & Maxwell, O. V. 1979, *ApJ*, 232, 541
- Gilberti, E. & Cambiotti, G. 2022, *MNRAS*, 511, 3365
- Glendenning, N. 2012, *Compact Stars: Nuclear Physics, Particle Physics and General Relativity*, Astronomy and Astrophysics Library (Springer New York)
- Goddard, P., Goldstone, J., Rebbi, C., & Thorn, C. B. 1973, *Nuclear Physics B*, 56, 109
- Guo, G. & Martínez-Pinedo, G. 2019, *ApJ*, 887, 58
- Guo, G., Martínez-Pinedo, G., Lohs, A., & Fischer, T. 2020, *Phys. Rev. D*, 102, 023037
- Hannestad, S. & Raffelt, G. 1998, *ApJ*, 507, 339
- Haskell, B. & Melatos, A. 2015, *International Journal of Modern Physics D*, 24, 1530008
- Haskell, B., Samuelsson, L., Glampedakis, K., & Andersson, N. 2008, *MNRAS*, 385, 531
- Hempel, M., Fischer, T., Schaffner-Bielich, J., & Liebendörfer, M. 2012, *ApJ*, 748, 70
- Hempel, M. & Schaffner-Bielich, J. 2010, *Nucl. Phys. A*, 837, 210
- Horowitz, C. J. 2002, *Phys. Rev. D*, 65, 043001
- Horowitz, C. J., Moniz, E. J., & Negele, J. W. 1985, *Phys. Rev. D*, 31, 1689
- Johnson, K. & Thorn, C. B. 1976, *Phys. Rev. D*, 13, 1934
- Kaltenborn, M. A. R., Bastian, N.-U. F., & Blaschke, D. B. 2017, *Phys. Rev. D*, 96, 056024
- Keegans, J., Fryer, C. L., Jones, S. W., et al. 2019, *MNRAS*, 485, 620
- Khosravi Largani, N., Fischer, T., & Bastian, N. U. F. 2023, arXiv e-prints, arXiv:2304.12316
- Khosravi Largani, N., Fischer, T., Sedrakian, A., et al. 2022, *MNRAS*, 515, 3539
- Klähn, T. & Fischer, T. 2015, *ApJ*, 810, 134
- Kurkela, A., Fraga, E. S., Schaffner-Bielich, J., & Vuorinen, A. 2014, *ApJ*, 789, 127
- Kuroda, T., Fischer, T., Takiwaki, T., & Kotake, K. 2022, *ApJ*, 924, 38
- Lasky, P. D. 2015, *PASA*, 32, e034
- Liebendörfer, M., Messer, O. E. B., Mezzacappa, A., et al. 2004, *ApJS*, 150, 263
- Liebendörfer, M., Mezzacappa, A., & Thielemann, F.-K. 2001, *Phys. Rev. D*, 63, 104003
- Liebendörfer, M., Rosswog, S., & Thielemann, F.-K. 2002, *ApJS*, 141, 229
- Lindquist, R. W. 1966, *Annals of Physics*, 37, 487
- Mezzacappa, A. & Bruenn, S. W. 1993a, *ApJ*, 405, 669
- Mezzacappa, A. & Bruenn, S. W. 1993b, *ApJ*, 410, 740
- Mezzacappa, A. & Bruenn, S. W. 1993c, *ApJ*, 405, 637
- Miller, M. C., Lamb, F. K., Dittmann, A. J., et al. 2019, *ApJ*, 887, L24
- Miller, M. C., Lamb, F. K., Dittmann, A. J., et al. 2021, *ApJ*, 918, L28
- Mirizzi, A., Tamborra, I., Janka, H.-T., et al. 2016, *Nuovo Cimento Rivista Serie*, 39, 1
- Mori, M., Suwa, Y., & Takiwaki, T. 2023, *Phys. Rev. D*, 107, 083015
- Most, E. R., Papenfort, L. J., Dexheimer, V., et al. 2019, *Phys. Rev. Lett.*, 122, 061101
- Nambu, Y. & Jona-Lasinio, G. 1961, *PhRv*, 122, 345
- Qian, Y. Z. & Woosley, S. E. 1996, *ApJ*, 471, 331
- Raduta, A. R., Oertel, M., & Sedrakian, A. 2020, *MNRAS*, 499, 914
- Riley, T. E., Watts, A. L., Ray, P. S., et al. 2021, *ApJ*, 918, L27
- Röpke, G., Blaschke, D., & Schulz, H. 1986, *Phys. Rev. D*, 34, 3499
- Ruderman, M. 1969, *Nature*, 223, 597
- Sagert, I., Fischer, T., Hempel, M., et al. 2009, *Phys. Rev. Lett.*, 102, 081101
- Sana, H., de Mink, S. E., de Koter, A., et al. 2012, *Science*, 337, 444
- Singh, N., Haskell, B., Mukherjee, D., & Bulik, T. 2020, *MNRAS*, 493, 3866
- Sotani, H. & Kojo, T. 2023, *Phys. Rev. D*, 108, 063004
- Sotani, H. & Kumar, B. 2021, *Phys. Rev. D*, 104, 123002
- Sotani, H., Kuroda, T., Takiwaki, T., & Kotake, K. 2017, *Phys. Rev. D*, 96, 063005
- Sotani, H., Maruyama, T., & Tatsumi, T. 2013, *Nucl. Phys. A*, 906, 37

- Sotani, H., Nakazato, K., Iida, K., & Oyamatsu, K. 2012, *Phys. Rev. Lett.*, 108, 201101
- Sotani, H. & Sumiyoshi, K. 2019, *Phys. Rev. D*, 100, 083008
- Sotani, H. & Takiwaki, T. 2016, *Phys. Rev. D*, 94, 044043
- Sotani, H., Takiwaki, T., & Togashi, H. 2021, *Phys. Rev. D*, 104, 123009
- Steiner, A. W., Lattimer, J. M., & Brown, E. F. 2010, *ApJ*, 722, 33
- Tauris, T. M., Langer, N., Moriya, T. J., et al. 2013, *ApJ*, 778, L23
- Tauris, T. M. & van den Heuvel, E. P. J. 2006, in *Compact stellar X-ray sources*, Vol. 39, 623–665
- Torres-Forné, A., Cerdá-Durán, P., Obergaulinger, M., Müller, B., & Font, J. A. 2019a, *Phys. Rev. Lett.*, 123, 051102
- Torres-Forné, A., Cerdá-Durán, P., Passamonti, A., & Font, J. A. 2018, *MNRAS*, 474, 5272
- Torres-Forné, A., Cerdá-Durán, P., Passamonti, A., Obergaulinger, M., & Font, J. A. 2019b, *MNRAS*, 482, 3967
- Typel, S., Röpke, G., Klähn, T., Blaschke, D., & Wolter, H. H. 2010, *Phys. Rev. C*, 81, 015803
- Wagoner, R. V. 1984, *ApJ*, 278, 345
- Warren, M. L., Couch, S. M., O'Connor, E. P., & Morozova, V. 2020, *ApJ*, 898, 139
- Watts, A. L., Krishnan, B., Bildsten, L., & Schutz, B. F. 2008, *MNRAS*, 389, 839
- Yagi, K. & Yunes, N. 2017, *Phys. Rep.*, 681, 1
- Yasutake, N., Lastowiecki, R., BeniĆ, S., et al. 2014, *Phys. Rev. C*, 89, 065803
- Zha, S., O'Connor, E. P., Chu, M.-c., Lin, L.-M., & Couch, S. M. 2020, *Phys. Rev. Lett.*, 125, 051102